Article

Lattice distortion enabling enhanced strength and plasticity in high entropy intermetallic alloy

Check for updates

H. Wang[1,12], P. Y. Yang[2,12], W. J. Zhao[1,3,12], S. H. Ma[1], J. H. Hou[4], Q. F. He[1,5], C. L. Wu[2], H. A. Chen[6], Q. Wang[7], Q. Cheng[8], B. S. Guo[1,9], J. C. Qiao[10], W. J. Lu [1][4], S. J. Zhao [1][1], X. D. Xu [1][6], C. T. Liu [1][1,11], Y. Liu [1][3] ✉, C. W. Pao [1][2] ✉ & Y. Yang [1][1,11] ✉

Intermetallic alloys have traditionally been characterized by their inherent brittleness due to their lack of sufficient slip systems and absence of strain hardening. However, here we developed a single-phase B2 high-entropy intermetallic alloy that is both strong and plastic. Unlike conventional intermetallics, this high-entropy alloy features a highly distorted crystalline lattice with complex chemical order, leading to multiple slip systems and high flow stress. In addition, the alloy exhibits a dynamic hardening mechanism triggered by dislocation gliding that preserves its strength across a wide range of temperatures. As a result, this high-entropy intermetallic circumvents precipitous thermal softening, with extensive plastic flows even at high homologous temperatures, outperforming a variety of both body-centered cubic and B2 alloys. These findings reveal a promising direction for the development of intermetallic alloys with broad engineering applications.

Intermetallic alloys possess exceptional strength, thermal stability, and creep resistance, making them promising for structural applications at high temperatures, such as in the aerospace and nuclear industries[1]. However, the poor plasticity of traditional intermetallic alloys at low temperatures due to a lack of sufficient slip systems and inadequate strain hardening poses a significant hurdle[1]. While intermetallic alloys may appear malleable at elevated temperatures, their strength typically declines precipitously as the homologous temperature approaches -0.5, limiting their utility[2]. Therefore, extensive research has been conducted to develop strong yet plastic intermetallic alloys[3], including

exploration of non-stoichiometric compositions for alloy design[4], synthesis of intermetallic matrix composites[5], and micro-alloying with non-metallic elements such as carbon or boron[6]. Despite these efforts, the fundamental issue to develop strong yet plastic intermetallic alloys still remains open.

To overcome the inherent brittleness faced by traditional intermetallics, a recent proposal for high-entropy intermetallic alloys (HEIAs) has emerged. In contrast to conventional alloys, HEIAs contain numerous principal elements, similar to multi-principal element random alloys or high-entropy alloys (HEAs)[7,8], while also featuring long-

[1]Department of Mechanical Engineering, City University of Hong Kong, Tat Chee Avenue, Kowloon Tong, Kowloon, Hong Kong, China. [2]Research Center for Applied Sciences, Academia Sinica, Taipei, Taiwan. [3]State Key Laboratory of Powder Metallurgy, Central South University, Changsha, Hunan, China. [4]Department of Mechanical and Energy Engineering, Southern University of Science and Technology, Shenzhen, Guangdong, China. [5]Institute of Materials Modification and Modeling, School of Materials Science and Engineering, Shanghai Jiao Tong University, Shanghai, China. [6]Department of Materials and Mineral Resources Engineering, National Taipei University of Technology, Taipei, Taiwan. [7]Laboratory for Microstructures, Institute of Materials, Shanghai University, Shanghai, China. [8]Centre for High Resolution Electron Microscopy, College of Materials Science and Engineering, Hunan University, Changsha, Hunan, China. [9]Institute of Advanced Wear & Corrosion Resistant and Functional Materials, Jinan University, Guangzhou, Guangdong, China. [10]School of Mechanics, Civil Engineering and Architecture, Northwestern Polytechnical University, Xi'an, Shanxi, China. [11]Department of Materials Science and Engineering, City University of Hong Kong, Tat Chee Avenue, Kowloon Tong, Kowloon, Hong Kong, China. [12]These authors contributed equally: H. Wang, P. Y. Yang, W. J. Zhao. ✉e-mail: yonliu@csu.edu.cn; cwpao@gate.sinica.edu.tw; yonyang@cityu.edu.hk

range chemical order and elemental random mixing. Even though the current focus of research in physical metallurgy has been the design of strong yet ductile HEAs by integrating multiple principal elements in a common lattice[9,10]; however, by fully embracing the "high entropy" notion, here we show that one can develop a single-phase HEIA capable of resisting precipitous strength softening and maintaining stable and extensive plastic flows at high homologous temperatures (e.g., 0.5–0.7), surpassing the mechanical properties of traditional inter-metallic alloys.

Results

Strength–plasticity synergy enabled by lattice distortion

In order to develop an alloy with both large lattice distortion and a stable lattice structure, we took into consideration the influence of large atomic size differences and electronic property variations. These factors contribute to the formation of a highly distorted lattice, which in turn enables promising properties[11]. Meanwhile, the inclusion of multiple principal elements in the alloy composition generally leads to higher ideal mixing entropy, thereby assisting in stabilizing the lattice and reducing free energy (known as the high-entropy effect)[12]. Based on these considerations, we designed our HEIA with a composition of $(CoNi)_{50}(TiZrHf)_{50}$ (at. %) to take advantage of the significant size and electronic property misfit among these five principal elements. In our previous work[13], we demonstrated the presence of superelasticity and the Elinvar effect in this alloy, attributed to lattice distortion. In this work, we aim to delve deeper into the influence of lattice distortion on the plasticity of $(CoNi)_{50}(TiZrHf)_{50}$. The electron backscatter diffraction (EBSD) and the X-ray diffraction (XRD) pattern (Fig. 1a), together with the scanning electron microscopy (SEM), scanning transmission electron microscopy (STEM) and energy-dispersive X-ray spectroscopy (EDS) analyses (Supplementary Figs. 1 and 2), all indicate that this alloy possesses a single-phase polycrystalline structure with B2 symmetry (space group: $Pm\bar{3}m$). Following ref. 13, we carried out geometric phase analyses (GPA) on defect-free lattices, which reveals heterogeneous lattice strains (Supplementary Fig. 3) with a fractal-like statistical distribution[14]. The lattice distortion within our intermetallic alloy is characterized by a high fluctuation of von Mises strain by atomistic simulations[13] and GPA (Supplementary Fig. 3), which exceeds those reported in the literature[14,15], as well as that of elemental metal Mo. It is important to note that, despite the similar size of Co and Ni, Co tends to form a B2 structure with Ti/Zr/Hf[16], while Ni tends to form more complex structures with these elements, such as the B19' Martensite phase in NiTi[17] and the oc8 structure in NiZr[18]. Therefore, the observed severe lattice distortion in our HEIA can also be attributed to the misfit of the crystalline structures in these two Co- and Ni-based pseudo-binary systems. This suggests that one can potentially manipulate the lattice distortion in our alloy simply by adjusting the ratio of Co to Ni. This intriguing topic is out of the scope of the current work but warrants further research. To study the plasticity of our alloy, we conducted uniaxial compression tests from room temperature (RT) to $\sim 0.9 T_m$, where T_m is the melting temperature ($= 1582 K$ as seen in Supplementary Fig. 4). As depicted in Fig. 1b, our HEIA exhibits a yield strength of $\sim 1.5 GPa$ with a plastic strain of $\sim 8\%$ at a strain rate of $1 \times 10^{-3} s^{-1}$ at RT. This compressive plasticity is about eight times that reported for conventional B2 alloys, such as NiAl[19] and CoTi[20], tested at strain rates of $1 \times 10^{-3} s^{-1}$ and $4.2 \times 10^{-4} s^{-1}$, respectively.

The electron channeling contrast imaging (ECCI) analysis reveals that the RT-deformed grains of the HEIA demonstrates an abundance of high-density planar slip bands (Supplementary Fig. 5a). We observed vein-like patterns on the fractured surface of our HEIA (Supplementary Fig. 5b), which is typical of amorphous alloys rather than crystalline ones[21,22]. Although the fracture of our HEIA releases a substantial amount of strain energy due to its high strength and elasticity[13], we did not observe the presence of molten droplets typically associated with adiabatic heating[23]. At 673 K, our HEIA exhibits excellent malleability

despite its high yield strength. The fracture surface of the HEIA then displays an expectedly ductile behavior, exhibiting dimples rather than vein-like patterns (Supplementary Fig. 5c). Comparative analyses of the temperature-dependent yield strength of our HEIA with other single-phase alloys possessing a body-centered cubic (BCC) or B2 symmetry reveals that our alloy surpasses all other BCC or B2 alloys for its strength, as shown in Fig. 1c (see Supplementary Table 1 for details). Unlike other alloys, our HEIA does not experience precipitous thermal softening at homologous temperatures between 0.5 and 0.7. Furthermore, our HEIA displays significant strain hardening and extensive plasticity even at the homologous temperature as high as ~0.7, in contrast to other BCC and B2 alloys, which typically suffer strain softening and may fracture at lower homologous temperatures, as shown in Fig. 1d (see Supplementary Table 2 for details).

Dislocation multiplicity and isotropic-like mechanical behavior

We conducted comprehensive microcompression tests on $(CoNi)_{50}(TiZrHf)_{50}$ with different crystal orientations and at varying temperatures to investigate the underlying deformation mechanisms. Utilizing the ion milling method[24], we fabricated micropillars measuring $1 \mu m$ in diameter and $2 \mu m$ in height (see Methods). As observed in Fig. 2a, the nominal stress–strain curves obtained from the micropillars with [100], [110], and [111] orientations are serrated and exhibit similar elastic stiffness and yield strength at RT, demonstrating weak elastic modulus and yield strength dependence on crystal orientation, a characteristic that considerably deviates from conventional crystalline alloys[25] (Fig. 2b and Supplementary Table 3). This can be attributed to severe lattice distortion found in our HEIA, which mitigates the atomic bonding difference along various crystal orientations, therefore imparting isotropic-like behavior to our alloy. The nominal stress–strain curves from the [111] oriented micropillars at different temperatures clearly show that our B2 alloy's serrated plastic flow at low temperatures becomes smooth with increasing temperature (Fig. 2c). This behavior is opposite to that of conventional BCC microcrystals, such as niobium[26], which exhibit enhanced plastic flow serrations at high temperatures. The occurrence of serrations, characterized by abrupt stress drops in stress–strain curves during micropillar tests, is primarily attributed to avalanches of dislocations that escape from a micropillar through its lateral surfaces[27,28]. These avalanches are closely associated with severe localization of plastic deformation, such as the formation of shear band-like structures in RT-deformed micropillars (Fig. 2l). Conversely, the absence of serrations at high temperatures implies a persistent dislocation pinning effect[28], which results in the formation of a dense dislocation forest instead of avalanches, as exemplified in the micropillar deformed at 673 K (Fig. 2o). We note that the elastic moduli obtained from microcompression are temperature insensitive, being consistent with the Elinvar effect reported in ref. 13, while the corresponding yield strengths decrease by 30% as the homologous temperature doubles (Fig. 2d). This trend agrees well with the conventional compression results (Fig. 1c).

Following postmortem TEM inspection of deformed micropillars, we identified two slip systems, namely {110} < 111> and {010} < 100 >, in $(CoNi)_{50}(TiZrHf)_{50}$ using $g \cdot b$ contrast analyses (where g represents the reciprocal lattice vector, and b the Burgers vector), as detailed in Supplementary Tables 4–6, and exemplified by Fig. 2e–g and Supplementary Figs. 6–8. This discovery is noteworthy because it shows that our HEIA possesses at least eight slip systems (compared to brittle B2 alloys like NiAl, which have fewer), making it more than capable of accommodating plastic flows in polycrystals. Furthermore, we measured the critical resolved shear stress (CRSS) for these slip systems, and found it to be 1235 ± 39 MPa for {110} < 111> and 1176 ± 245 MPa for {010} < 100> (see Supplementary Table 3). The average CRSS values for the two types of slip systems in our HEIA are very close, differing within only 5% (Fig. 2h), enabling the simultaneous activation of both systems.

This stands in contrast to conventional B2 alloys, where the difference in CRSS between slip systems, such as $(1\bar{1}2)[\bar{1}11]$ and $(001)[010]$, can reach up to 500% (as seen in NiAl[29]), resulting in the dominance of the $(001)[010]$ slip system. Here we also note that, despite the similarities between our HEIA and an amorphous structure, such as property isotropy shown in Fig. 2b, the number of slip systems is not reduced. This is not a contradiction, since our HEIA still remains a crystalline structure, not amorphous, which means that crystalline defects, such as dislocations, are still carriers of plasticity.

To investigate plastic flows at different temperatures, we conducted in situ STEM microcompression tests at both RT (Supplementary Movie 1) and 573 K (Supplementary Movie 2) (see "Methods").

Figure 2i shows an annular bright-field STEM (ABF-STEM) image of a single-crystal sample deformed to 20% strain at RT, revealing the active slip system to be of {010}<100> type. Interestingly, with increasing plastic strain, amorphization occurred within slip bands (Figs. 2j–n and Supplementary Movie 1) without any detectable elemental segregation at a length scale of 10 nm (Methods, Supplementary Fig. 9). This behavior was also observed during the deformation a bulk polycrystalline sample at RT (Supplementary Fig. 10), implying that the observed phase transition is a result of moving defects. Under large plastic deformation, extensive amorphization occurred in slip bands in our HEIA, which can lead to sudden fracture as a result of deformation induced instability in amorphous structures. However, at
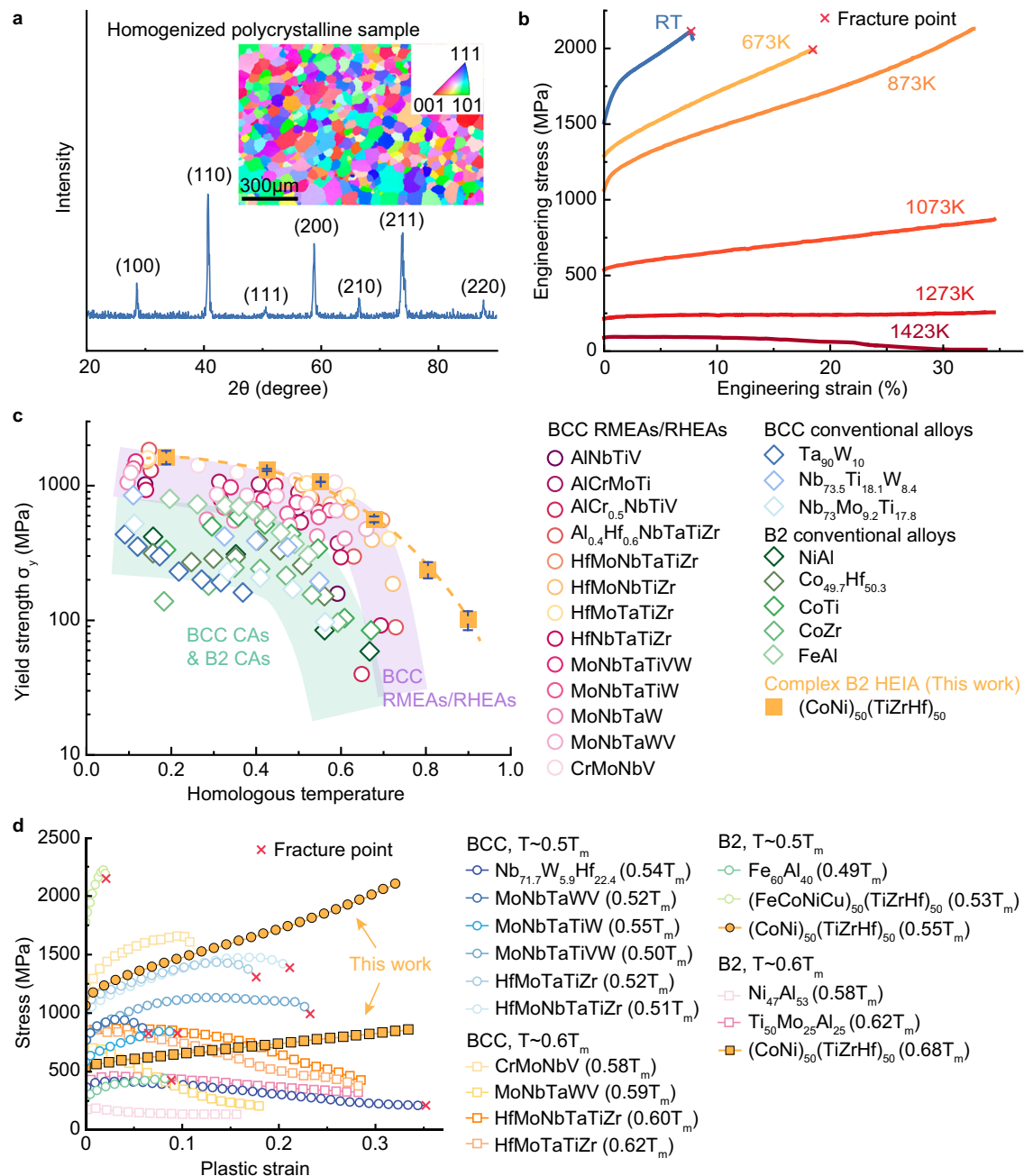

Fig. 1 | Microstructure and mechanical properties of the polycrystalline (CoNi)$_{50}$(TiZrHf)$_{50}$ alloy. a The XRD pattern and EBSD image (the inset) of the homogenized polycrystalline (CoNi)$_{50}$(TiZrHf)$_{50}$. **b** The engineering stress–strain curves obtained at different temperatures. **c** The comparison of compressive yield strengths (σ_y) measured for a variety of alloys at different homologous temperatures (T/T_m). Note that RMEAs = refractory medium entropy alloys, RHEAs = refractory high-entropy alloys and CAs=conventional alloys. Error bars are the standard deviation. **d** The plots of the flow stress versus plastic strain for BCC alloys, B2 alloys, and (CoNi)$_{50}$(TiZrHf)$_{50}$ at 0.5T_m and 0.6T_m. Source data are provided as a Source Data file.

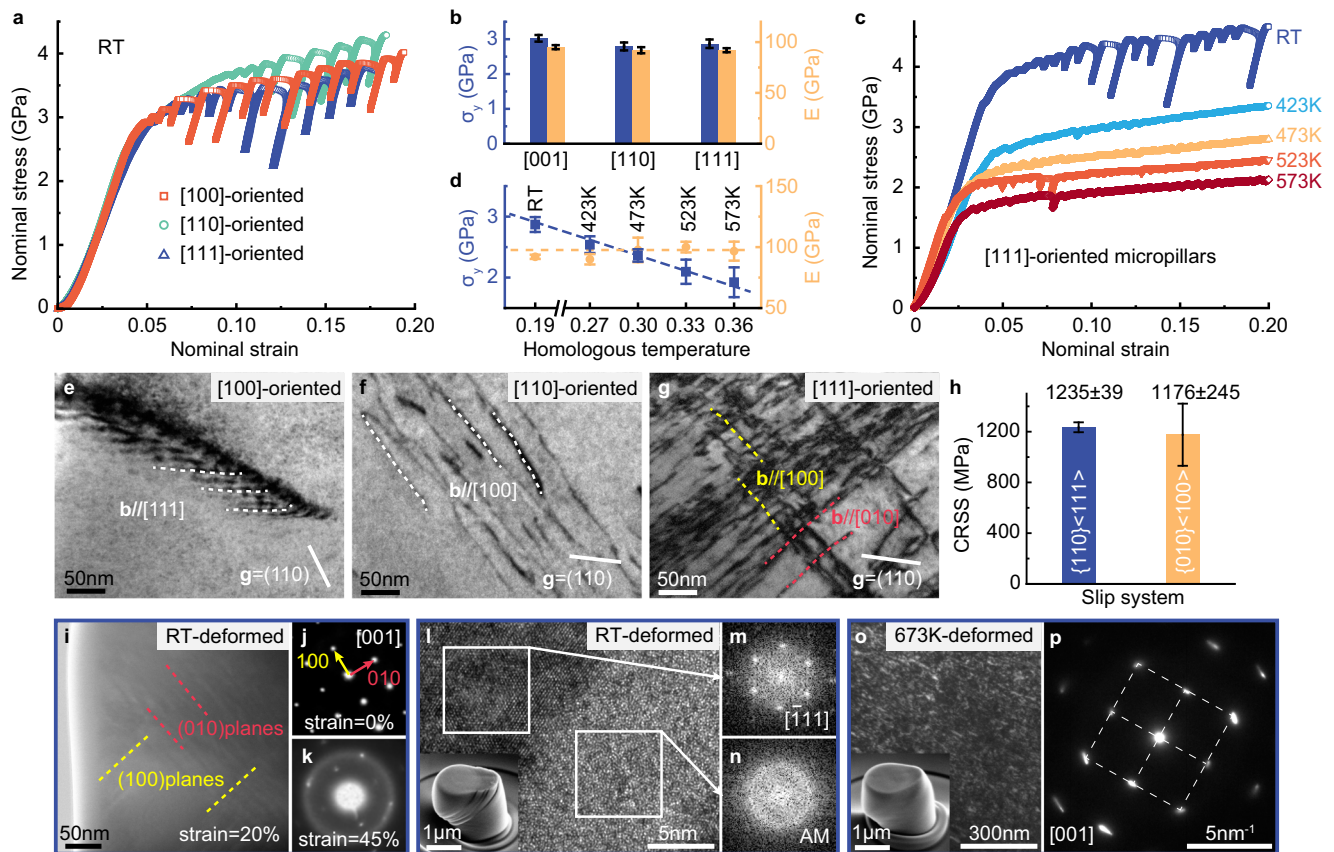**Fig. 2 | Mechanical behavior in the single-crystal (CoNi)$_{50}$(TiZrHf)$_{50}$ alloy. a** The nominal stress–strain curves of the micropillars with the orientation of [100], [110], and [111] obtained at RT. **b** The yield strength σ_y and Young's modulus E of the micropillars measured for different crystal orientations at RT. **c** The nominal stress–strain curves of the [111]-oriented micropillars obtained at different temperatures. **d** The σ_y and E measured for the [111]-oriented micropillars at different temperatures. Dislocations with their Burgers vector **b** parallel to [111] observed in the deformed [001] single crystal (**e**), **b** parallel to [100] observed in the deformed [110] single crystal (**f**), and **b** parallel to [100] and [010] observed in the deformed [111] single crystal (**g**). **h** The CRSS measured for the two types of slip systems. **i** The in situ ABF-STEM image of a deformed single-crystal sample with the strain of 20% at RT. The red and yellow dashed lines mark two different slip systems. **j** The in situ selected area electron diffraction (SAED) pattern taken before deformation (strain = 0%). **k** The in situ SAED pattern taken at the strain of 45%. **l** The high-resolution TEM (HRTEM) image of the partially amorphized micropillar deformed at RT. The inset shows the SEM image of the sample after deformation with the strain of 30%. The crystal and amorphous structures are characterized through FFTs, as shown in (**m**, **n**), respectively (AM = amorphous). **o** The centered dark-field TEM image of a micropillar deformed at 673 K. The inset shows the SEM image of the deformed sample. **p** The SAED pattern obtained from o. Error bars in (**b**, **d**, **h**) are the standard deviation. Source data are provided as a Source Data file.

temperatures above 573 K, deformation localization gradually diminished without detectable amorphization (Supplementary Fig. 11 and Supplementary Movie 2). Instead, we observed extensive and densely populated dislocations (Fig. 2o), which can explain the smooth and homogeneous plastic flows observed in bulk and microcompression (Fig. 2b). Intriguingly, despite the further distortion caused by dislocation accumulation (Fig. 2o, p), the distorted crystalline lattice was able to withstand extensive plastic flows. The tolerance of such severe lattice distortion may be attributed to the combined effects of "high mixing entropy"[12] and the non-close-packing character of the B2 structure[30].

To reveal the atomic origins of the elastoplasticity in our HEIA, we developed a multi-component interatomic potential by training a machine learning (ML) enabled interatomic potential model with the data from thousands of first-principles calculations for the Co–Ni–Ti–Zr–Hf system (see "Methods" and Supplementary Fig. 12 for details). This enabled us to perform large-scale molecular dynamics (MD) simulations to study the deformation behavior of our model (CoNi)$_{50}$(TiZrHf)$_{50}$ system (see "Methods"). Our calculated elastic constants at different temperatures, as shown in Supplementary Fig. 13, exhibit minimal temperature dependence and are consistent with our experimental data (Fig. 2d). In addition, we calculated

the elastic constants for different crystalline orientations, and found that the magnitude of the elastic constants is insensitive to orientation, with a Zener anisotropy ratio close to unity (Supplementary Fig. 13a), which agrees with our experimental findings (Fig. 2b). We also simulated the gliding behavior of the two types of dislocations (i.e., {110}<111> and {010}<100>) identified in our experiments (see "Methods"). Figure 3a, b depicts the rugged local stress landscape at 300 K that a screw (Fig. 3a) and edge (Fig. 3b) dislocation must traverse while gliding through the severely distorted lattice. The movement of both types of dislocations can become "pinned" in regions of high compressive stress, causing their trajectories to become wavy and tortuous, regardless of their initial character (see Supplementary Movie 3 and Supplementary Movie 4). Our MD simulations enabled us to compute the ratio of the velocity of screw-to-edge dislocations in (CoNi)$_{50}$(TiZrHf)$_{50}$, which was -0.6 at 300 K (Supplementary Fig. 14). Interestingly, this velocity ratio is much higher than that (-0.2) in brittle BCC metals at low temperatures, such as tungsten[31], but is similar to those triggering the brittle-to-ductile transition in BCC metals[31]. This phenomenon can be attributed to the sluggish dislocation movement induced by the highly fluctuating stress field, which effectively reduces the disparity in velocity between screw and edge dislocations.
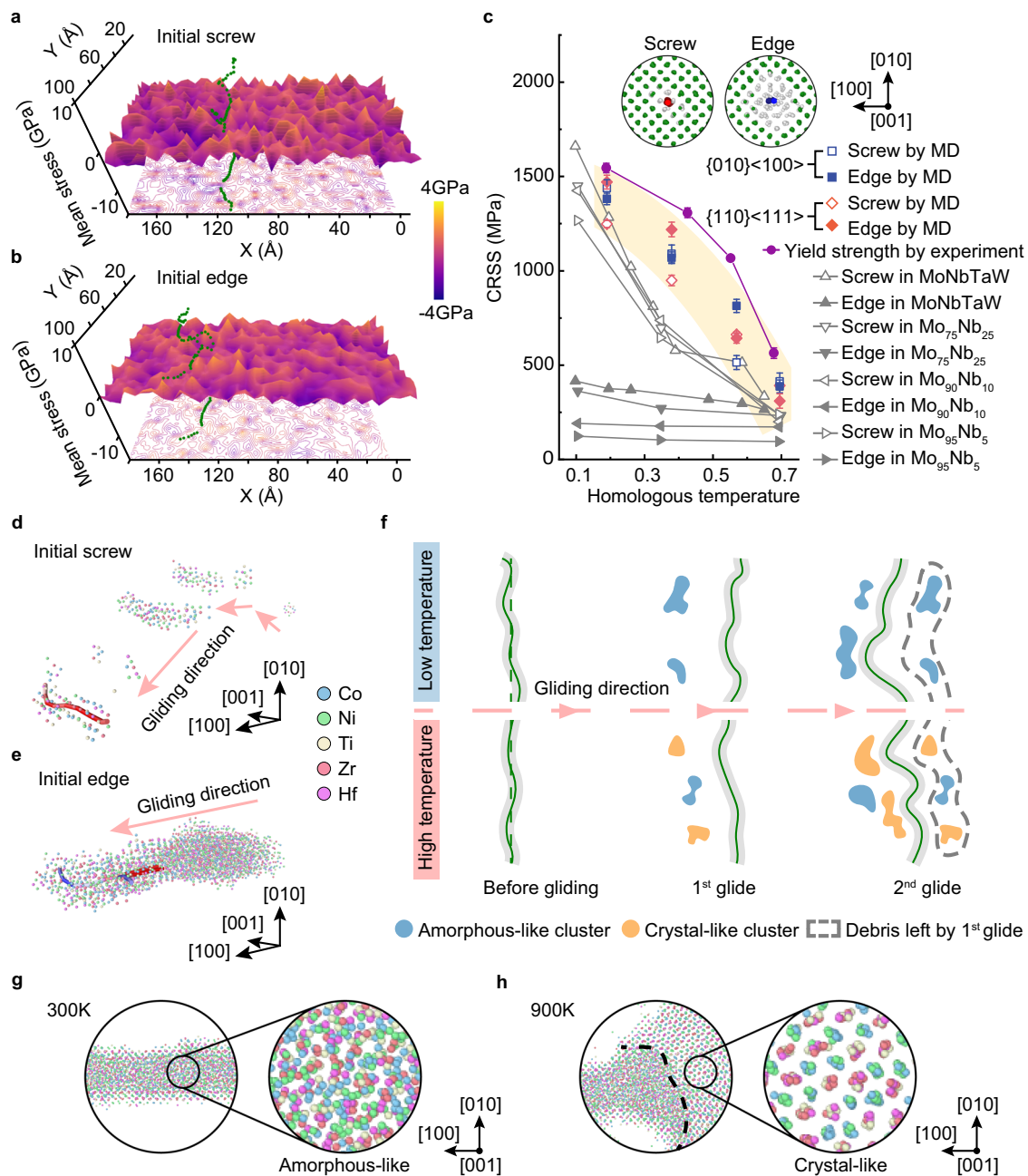
Fig. 3 | Understanding plasticity mechanisms in (CoNi)$_{50}$(TiZrHf)$_{50}$ through atomistic simulations. The 3D visualization of a {110} < 100> dislocation gliding through the lattice distortion-induced atomic stress field with the initial character of the screw (**a**) and edge (**b**). **c** The CRSS obtained via MD simulations for screw and edge dislocations in (CoNi)$_{50}$(TiZrHf)$_{50}$ at different homologous temperatures for both {010} < 100> and {110} < 111> slip systems, in comparison with those of BCC refractory alloys also obtained from MD simulations[59]. Note that the yield strengths of (CoNi)$_{50}$(TiZrHf)$_{50}$ experimentally measured at different temperatures (Fig. 1b) are also included for comparison. The yellow shading captures the general trend of CRSS for eye guidance. The insets show the front views of the typical {010} < 100> screw (colored in red) and edge dislocation (colored in blue) after energy relaxation showing an extended dislocation-affected zone surrounding the dislocation core. Here green and gray balls represent atoms with B2 and non-B2 packing,

respectively. The remnant non-B2 atomic clusters formed along the trail of a gliding {010} < 100> dislocation with the initial character of screw (**d**) and edge (**e**). Note that atoms with B2 packing are hidden here for clarity. **f** The schematic illustration of the dynamic strengthening mechanism enabled by dislocation gliding induced local structural transition in a severely distorted crystal. The dotted green line represents a pristine straight dislocation line before energy relaxation and the gray shade represents the dislocation-affected zone as revealed in the inset of (**c**). **g** The formation of amorphous-like regions after multiple gliding of {010} < 100> edge dislocations in our MD simulations at 300 K. **h** The formation of dislocation gliding induced amorphous- and crystal-like regions at 900 K. The dotted line separates the amorphous- and crystal-like regions. Source data are provided as a Source Data file.

In order to gain further insight into the behavior of screw and edge dislocations in the heavily distorted B2 structure, we analyzed the local atomic structures surrounding both dislocation cores (see "Methods"). As shown in the inset of Fig. 3c, these structures are highly distorted and exhibit non-B2 packing. Interestingly, the dislocation-

affected zone is more extensive for the edge dislocation than for the screw dislocation. To quantify the CRSS of the dislocations for both {010} < 100> and {110} < 111> slip systems across a variety range of temperatures, we conducted extensive MD simulations (Supplementary Fig. 15) and found that the trend of the calculated CRSS values are

in good agreement with that of the measured yield strengths (Fig. 1c). The CRSS values for the {010}<100> and {110}<111> slip systems are similar, consistent with our experimental findings (Fig. 2h), which implies equal contributions from these two active slip systems to the observed strength softening. Furthermore, the average CRSS value for the screw dislocation is slightly lower than that for the edge dislocation, regardless of the slip system. As discussed in refs. [32–34], the high CRSS for edge dislocations can effectively mitigate thermal softening caused by diffusion-controlled plasticity in BCC metals[2,35]. This explains why our HEIA retains high strength at high homologous temperatures of 0.5–0.7 (Fig. 1c).

Discussion

In conventional face-centered cubic (FCC) and BCC metals, atomic structures remain intact after the passage of dislocations. However, in our HEIA, the highly distorted crystal structure becomes unstable as dislocations of either a screw or edge character sweep through (see Fig. 3d, e). This structural instability can be attributed to the disruption of local chemical order by the dislocations. For instance, the formation of an antiphase region due to dislocation dissociation is observed in a pair of 1/2<111> dislocations (Supplementary Fig. 16), along with extensive dislocation core structures of <100> dislocations, as shown in the inset of Fig. 3c. It is worth noting that, in addition to destabilizing the lattice, the dissociation of dislocations with antiphase regions can also planarize the dislocation core structure[36]. This planarization enables <111> dislocations to move more freely within the lattice, resulting in better plasticity compared to alloys where only <100> dislocations are activated. Regardless of the dislocation Burgers vectors, we found that dislocation gliding became more difficult along the trail of passing dislocations due to the formation of debris resulting from structural disturbance, as depicted in Fig. 3f. At low temperatures (300 K and 600 K), dislocation gliding disturbs the distorted crystal lattice and even causes local amorphization (Fig. 3g), consistent with our experimental observations (Fig. 2i–n and Supplementary Fig. 10). At elevated temperatures (900 K), the structural disturbance manifests as the formation of local crystal-like order distinct from the original B2 packing (Fig. 3h), which might be attributed to the structural relaxation of the otherwise amorphized regions at low temperatures. In our simulations, we found that these local crystal-like ordering acts as an impediment to subsequent dislocation gliding, leading to strain hardening at high temperatures. As further verification, we fabricated (CoNi)$_{50}$(TiZrHf)$_{50}$ films through magnetron sputtering, which is amorphous rather than B2 due to the ultrahigh effective cooling rate (see "Methods"). We measured their glass transition temperature through nano-calorimetry (Supplementary Fig. 17). Our experimental results indicate that the glass transition temperature of the (CoNi)$_{50}$(TiZrHf)$_{50}$ amorphous structure is about 540 K at a heating rate of 10 K/min. It is, therefore, likely that the lack of detectable amorphization as the temperature increases above 573 K (Supplementary Fig. 11) can be attributed to the local structural relaxation.

In summary, we report a plastic yet strong HEIA in this study. The severe lattice distortion causes the elastic constants of this HEIA to be insensitive to crystal orientation, resulting in high strength and dislocation multiplicity that are rarely observed in conventional B2 lattice. Dislocation-mediated plasticity triggers local structural transition in the wake of passing dislocations, leading to amorphization at low temperatures and dynamic hardening at high temperatures, which stabilizes plastic flows even at very high homologous temperatures. Moreover, the lattice distortion in our HEIA imparts similar resistance to the gliding of both screw and edge dislocations, resembling the behavior of ductile FCC metals rather than brittle BCC or B2 metals. This combination of properties makes the (CoNi)$_{50}$(TiZrHf)$_{50}$ HEIA promising for various structural and functional applications, including acoustic cloaks made of elastic isotropic materials[37], turbine blades in aerospace/aircraft industries, exhaust valves in automotive industries and etc.[1,38,39].

Methods

Sample preparation

The polycrystalline samples of high-entropy intermetallic alloy (CoNi)$_{50}$(TiZrHf)$_{50}$ (at. %) were prepared through arc-melting with high-purity raw materials (> 99.9 wt. %) under a Ti-gettered argon atmosphere. The ingots were remelted at least five times to ensure the chemical homogeneity, and then dropped cast into a $5 \times 10 \times 60$ mm^3 plate copper mold. The samples were homogenized at 1000 °C for 24 h followed by water quenching with cooling rate estimated to be hundreds of Kelvin per second[40]. The amorphous thin films were deposited on NaCl substrates by magnetron sputtering, using a target with nominal composition of 25Co–25Ni–16.67Hf–16.67Ti–16.67Zr (at. %). After deposition, the alloy NaCl system was immersed into deionized water. Eventually, the NaCl substrates were dissolved and the deposited thin films were collected for further characterization.

Structural and compositional characterization

The crystalline phase was identified using an XRD instrument (Rigaku Smartlab). The topography characterization was performed on a SEM (FEI Quanta 450 FEG). The crystalline orientation was determined by an EBSD (EDAX TSL) equipped in FEI Quanta 450 FEG-SEM. Based on the EBSD results, micropillars were fabricated within grains exhibiting [100], [110] or [111] orientations using a focused-ion beam (FIB) system integrated into a FEI SEM/FIB setup. The high-angle annular dark-field scanning transmission electron microscopy (HAADF-STEM) observations were conducted on Titan Themis G2 and JEM-ARM300F Cs-corrected microscopes operated at 300 kV. The ABF-STEM observations of in situ microcompression and the characterizations of elemental distribution were performed on Talos F200X G2 microscope equipped with energy-dispersive X-ray spectroscopy (EDS), operating at 200 kV. The semi-collection angle ranges for HAADF-STEM and ABF-STEM observations are 48 (inner)–200 (outer) mrad and 14 (inner)–23 (outer) mrad, respectively. The spatial limit (R) of TEM-EDS was estimated as $R = (d + R_{max})/2$, where d is spot size and $R_{max} = \sqrt{d^2 + b^2}$. The beam spread ($b$) is calculated as $b = 8 \times 10^{-12} \frac{Z}{E_0} N_v^{\frac{1}{2}} t^{\frac{3}{2}}$, where E_0 is beam energy, Z is atomic number, N_v is the number of atoms per unit volume and t is the sample thickness[41]. The dislocation characterizations and HRTEM observations were performed on a JEOL 2100 F TEM equipment. The TEM specimens of polycrystalline (CoNi)$_{50}$(TiZrHf)$_{50}$ were prepared by mechanical grinding and ion milling (PIPS II System, Gatan). The TEM specimens of single-crystal (CoNi)$_{50}$(TiZrHf)$_{50}$ were prepared using FIB. The geometric phase analysis was carried out via the open-source program Strain++[42].

Mechanical and thermal properties characterization

The uniaxial compression tests of polycrystalline (CoNi)$_{50}$(TiZrHf)$_{50}$ alloy at different temperatures were performed on a Gleeble 3180D thermal simulation testing machine at a strain rate of 10^{-3} s^{-1}. The compression samples with a diameter of 4 mm and an aspect ratio of about 2 were prepared by wire cutting, followed by mechanical grinding and polishing to a mirror finish. The sample temperature was controlled by a K-type thermocouple welded to the samples. In the tests at 400 °C, 600 °C, and 800 °C, graphite flakes with high-temperature lubricant were inserted between samples and platens. In the tests at 1000 °C and 1150 °C, additional tantalum sheets were added between graphite flakes and platens for lubrication and anti-adhesion. Here we should note that the plastic strain of our alloy obtained at room temperature could reach 27% if we tested the samples on a testing machine with a high machine stiffness. However, such variability disappeared with increasing temperature. A similar machine stiffness effect was also observed on amorphous alloys[43]. Again, this supports the view that fracture of our alloy at low temperatures may

take place within the amorphized regions. Micropillar compression tests were performed on a Hysitron TI 950 TriboIndenter system equipped with a high-temperature stage under an argon atmosphere.

The differential scanning calorimetry (DSC) instrument (TGA/DSC 3 + , METTLER-TOLEDO) was used to characterize the thermal properties of bulk polycrystalline specimens, which were placed in an alumina crucible and tested under argon atmosphere. The testing temperature increased from 30 to 1600 °C at 10 °C/min. The flash-DSC technique was applied to the amorphous thin films under argon atmosphere, using a METTLER-TOLEDO Flash-DSC 2 equipment. The glass transition temperatures (T_g) measured at different heating rates (φ, 1000 K/min, 4000 K/min, 8000 K/min, and 10,000 K/min) were fitted to Vogel−Fulcher−Tamman (VFT) relation: $\ln(\varphi) = \ln(B) - \frac{DT_0}{T_g - T_0}$, where B, D, and T_O are fitting parameters[44].

Bispectrum and SNAP potential

The spectrum neighbor analysis potential (SNAP)[45] has been utilized in ML energy models to capture the complex interactions between atoms. In the SNAP model, bispectrum components are employed to describe the atomic chemical environment. To begin with, the neighbor density of an atom i at coordinates r can be expressed as a sum of Dirac functions located in a three-dimensional space within the cutoff distance R_{cut}:

$$\rho_i(r) = \delta(r) + \sum_{r_{ij} < R_{cut}} f_c\left(r_{ij}\right) \omega_{atom}^j \delta\left(r - r_{ij}\right) \qquad (1)$$

where r_{ij} is the vector joining the position of the central atom i to neighbor atom j. The switch function $f_c\left(r_{ij}\right)$ ensures a smooth decay for the neighbor to zero at cutoff and the ω_{atom}^j is the dimensionless atomic weights to distinguish different atom types. This density function can be further expanded to a 4D hyperspherical harmonics basis $U_{m,m'}^j$:

$$\rho_i(r) = \sum_{j=0,\frac{1}{2},\cdots}^{\infty} \sum_{m=-j}^{j} \sum_{m'=-j}^{j} u_{m,m'}^j U_{m,m'}^j \qquad (2)$$

Because the coefficients $u_{m,m'}^j$ are complex values and not invariant under rotation, the following scalar triple products of $u_{m,m'}^j$, namely, the bispectrum components are utilized as descriptors instead.

$$B_{j1,j2,j} = \sum_{m_1,m_1'=-j_1}^{j_1} \sum_{m_2,m_2'=-j_2}^{j_2} \sum_{m,m'=-j}^{j} \left(u_{m,m'}^j\right)^* H_{j_2 m_2 m_2'}^{jmm'} u_{m_1 m_1'}^{j_1} u_{m_2 m_2'}^{j_2} \qquad (3)$$

where the constants $H_{j_2 m_2 m_2'}^{j_1 m_1 m_1'}{}^{jmm'}$ are the Clebsch-Gordan coefficients. In bispectrum, the j, j_1, and j_2 values require to be truncated at j_{max}. In this study, the order of four ($j_{max} = 4$) is chosen, which gives a total of 55 projected components. Under the SNAP model, the system energy and atomic forces are represented by a linear summation of the bispectrum components and their gradients, respectively:

$$E_{SNAP} = \sum_{i=1}^{N} \beta_0^{\alpha_i} + \sum_{i=1}^{N} \sum_{k=\{j,j_1,j_2\}} \beta_k^{\alpha_i} B_k^i = N\beta_0 + \beta \cdot \sum_{i=1}^{N} B^i \qquad (4)$$

$$F_{SNAP}^j = -\nabla_j E_{SNAP} = -\beta \cdot \sum_{i=1}^{N} \frac{\partial B^i}{\partial r_j} \qquad (5)$$

where α_i specified the atom i with type α, the β is the vector of SNAP coefficients and β_O is the constant energy contribution for each atom.

Training procedure

The training workflow of the ML energy model is depicted schematically in Supplementary Fig. 11a. To enhance the effectiveness of a potential, it is crucial to have diverse training data that encompasses a wide range of atomic local environments. In order to capture the characteristics of atomic local environments in complex multi-component alloy materials, the composition of the training set focuses on sampling diverse element permutation configurations of the crystalline structure. The B2 and BCC bulk structure of $(CoNi)_{50}(TiZrHf)_{50}$ with hydrostatic strains were randomly sampled in a range from −20 to +20%. To better capture the effects of cell distortion and phase transition in the BCC structure, we included HCP/BCC bicrystal structures in our training set. This allowed us to more accurately describe the behavior of the BCC phase and its response to various conditions. For each B2 structure, we randomly exchanged the (Co−Ni) and (Ti−Zr−Hf) atoms within their respective sublattice sites. In the case of BCC structures, we further exchanged less than 10% of the Zr atoms to the (Co−Ni) sublattice, based on elemental mapping results obtained from STEM-EDS[13]. In above configurations, the image information, such as cell-matrix, system energy, atomic forces, and coordinates, has been obtained through single-point energy calculations by using density functional theory (DFT). For each bicrystal structure, the geometry optimization has firstly been carried out before capturing the image information. Over 3000 configurations labeled with DFT energies and atomic forces were collected, and -10% of the configurations collected were extracted from the pool for trained model validation.

Once the DFT data set was prepared, the SNAP coefficients $\{\beta_0, \beta\}$ and hyperparameters (namely, atomic weights, $\{w\}$, and radius cutoff, $\{R_{cut}\}$) were trained via the following two-step iterative approach as illustrated in Supplementary Fig. 11a:

(a) Determination of SNAP coefficients: the SNAP coefficients were determined by the linear least square method mapping the bispectrum components of training images computed based on a hyperparameter set $\{w^n\}$, and $\{R_{cut}^n\}$, to respective energies and atomic forces.

(b) Hyperparameter optimization: the Bayesian algorithm[46] was utilized to minimize the loss function $l(\{w\}, \{R_{cut}\})$ defined as the weighted sum of the root-mean-square deviation (RMSD) of the energies and atomic forces between the SNAP prediction and DFT results in the above training data.

$$\left(\ell\{w\}, \{R_{cut}\}\right) = W_E RMSD\left(E_{\{w\},\{R_{cut}\}}^{SNAP}, E^{DFT}\right) + W_F RMSD\left(F_{\{w\},\{R_{cut}\}}^{SNAP}, F^{DFT}\right) \qquad (6)$$

where W_E and W_F are the weighting factors for the energy and atomic forces and were set to 100 and 1, respectively.

(c) A hyperparameter set $\{w^{n+1}\}$, and $\{R_{cut}^{n+1}\}$ for the next iteration were determined from the Bayesian optimizer. The whole training procedures were repeated until the loss function converged.

DFT calculations

The first-principles calculations based on DFT were utilized to generate training data. All calculations were performed by using Vienna ab initio simulation package (VASP)[47,48] with the all-electron projected augmented wave (PAW) pseudopotential[49]. The Brillouin zone was sampled by the Monkhorst−Pack method[50] with a grid of $2 \times 2 \times 3$ Γ-centered k-point. The electronic occupancies were described by the Methfessel−Paxton method with a 0.2 eV of smearing width. The kinetic-energy pseudopotentials were employed together with 400 eV cutoff energy for plane waves. The convergent tolerance of energies and forces were set to 10^{-5} eV and 0.02 eV/Å, respectively.

Validation of ML energy model

Supplementary Fig. 11b, 11c displays the energy and atomic force parities between the trained SNAP model and the DFT calculations for both the training images (red dots) and the validation images (green dots). The root-mean-square errors (RMSE) of potential energy and atomic force are less than 10.2 meV/atom and 0.327 eV/Å, respectively. Note that all three components of each atomic force were included in the plots mentioned above. Supplementary Fig. 11d depicts the atomic force direction parities between the SNAP model and DFT results. Most of the atomic force directions predicted by the SNAP model deviate from those obtained by the DFT calculations by less than 20°. Therefore, the atomic forces from the SNAP model trained using both energy and forces exhibit very good agreement with those obtained from the DFT calculations.

Next, we proceeded by constructing a bulk model of $(CoNi)_{50}(TiZrHf)_{50}$ alloy with B2 crystalline structure. The equilibrated structure was obtained from ab initio molecular dynamics (AIMD) and the classical MD combine with the SNAP model, respectively. Both MD simulations were carried out using the canonical ensemble with system temperature set to 300 K. Supplementary Fig. 11e shows the radial distribution function (RDF) of equilibrated structures that obtained from AIMD and MD, respectively. The position of intensive peaks in the RDFs of both equilibrated structures match perfectly, indicating that the SNAP model can successfully describe interatomic distances in such complex chemical environments. We also conducted MD simulations of the bulk model at three different temperatures, namely 300 K, 600 K, and 900 K. The computed linear thermal expansion coefficient was 12.6×10^{-6} K^{-1}, which is in excellent agreement with the experimental measurement of 11.4×10^{-6} K^{-1} (see ref. [13]). These findings demonstrate that our ML energy model can accurately predict the energies and structures of $(CoNi)_{50}(TiZrHf)_{50}$ alloy, obviating the need for computationally expensive DFT calculations.

To further confirm the superior energetics of the B2 structure compared to the BCC structure, we conducted Monte Carlo (MC) simulations with unrestricted lattice site swapping moves. In these simulations, site swapping moves were not confined to the (Co–Ni) and (Ti–Zr–Hf) sublattices. The MC simulations were performed at temperatures of 300 K and 900 K, utilizing the trained ML potential. In each MC simulation, trial moves consisted of site swapping followed by structure optimization to account for lattice distortions. The MC simulations were carried out for 5×10^{5} MC steps on our HEIA system comprising 7680 atoms. Throughout the simulations, no atom-swapping events between the (Co–Ni) and (Ti–Zr–Hf) sublattices were observed.

Elastic isotropy

To examine the elastic isotropy property, we performed MD simulations to compute the elastic constant for a single-crystal B2-$(CoNi)_{50}(TiZrHf)_{50}$ alloy at elevated temperatures (i.e., 300, 600, and 900 K). During the simulation, the system undergoes a finite tensile deformation under the NVT ensemble, and the change in the average stress tensor is measured to calculate elastic moduli. The Zener anisotropy ratio (A_Z) was calculated using $A_Z = 2C_{44}/(C_{11}-C_{12})$. For a conventional cubic system, elastic tensor (C_{ij}) and elastic compliance constants (S_{ij}) satisfy the following relations[51]:

$$S_{11} = \frac{C_{11} + C_{12}}{(C_{11} - C_{12})(C_{11} + 2C_{12})} \tag{7}$$

$$S_{12} = \frac{-C_{12}}{(C_{11} - C_{12})(C_{11} + 2C_{12})} \tag{8}$$

$$S_{44} = \frac{1}{C_{44}} \tag{9}$$

The Yong's modulus for $\{h\,k\,l\}$ plane (E_{hkl}) can be obtained by the following equation[51]:

$$\frac{1}{E_{hkl}} = S_{11} - 2\left[(S_{11} - S_{12}) - \frac{1}{4}S_{44}\right]\left[\frac{h^2k^2 + k^2l^2 + l^2h^2}{(h^2 + k^2 + l^2)}\right] \tag{10}$$

The distributions of E_{hkl} obtained as a function of three orthogonal axes ([001], [010], and [100]) are plotted in Supplementary Fig. 12.

Shear simulation

We calculated the CRSS of B2-$(CoNi)_{50}(TiZrHf)_{50}$ alloys containing a single dislocation at different temperatures using LAMMPS[52] to investigate the strengthening mechanism arising from different dislocation types. For this purpose, we inserted a single straight edge or screw dislocation with a Burgers vector of **b** = [100] on {010} planes (namely, {010} < 100 > slip system) and **b** = [111] on {110} planes (namely, {110} < 111 > slip system) in the perfect B2-$(CoNi)_{50}(TiZrHf)_{50}$ alloy respectively, using ATOMSK[53]. Even though there are slight differences in system dimensions and atom numbers between the two dislocation models due to the different atomic stacking along different crystalline orientations, we ensured that both systems are sufficiently large along the slip direction and the length of dislocation lines is comparable. For the {010} < 100 > dislocations, the system was constructed with the orientation of X = [100], Y = [010], and Z = [001] (~ 33 Å). For the {110} < 111 > dislocations, the orientation of the system was: X = [11$\bar{2}$], Y = [1$\bar{1}$0], Z = [$\overline{111}$] (~ 37 Å). The dislocation is identified by the Dislocation Analysis (DXA)[54] and atoms are colored according to Polyhedral Temperature Matching (PTM)[55] using OVITO[56]. Screw dislocation was colored red, and edge dislocation was colored blue.

For shear simulation, the simulation box was divided into four regions: vacuum layers, fixed layer, thermostat layer, and mobile layer. Before the shear simulation, energy minimization and relaxation under the Nose-Hoover thermostat for 50 ps was performed to equilibrate the system to a desired temperature. The temperature dependence of CRSS was evaluated at 300 K, 600 K, 900 K, and 1100 K. The deformation-control method is implemented by applying a shear strain with a strain rate of 5×10^{8} s^{-1} to the fixed layer. During deformation, the thermostat layer was controlled by an NVE ensemble, and the mobile layer was under a NVT ensemble. The shear stress–strain curves obtained in each dislocation system are presented in Supplementary Fig. 14. The CRSS values were determined as the average flow stress after yield in the stress–strain curves[57].

Atomic stress field and CRSS

To identify dislocation slipping behaviors, it is necessary to acquire the stress field, particularly the normal stress surrounding the slip plane. The atomic stresses were calculated based on the virial stress tensor and Voronoi volume[58]. The virial stress tensor for atom i is given by the following formula, where a and b take on values x, y, and z to generate the components of the tensor:

$$S_{iab} = -mv_av_b - W_{iab} \tag{11}$$

where the first and second terms represent the kinetic energy and virial contribution for atom i, respectively. The virial contribution W_{iab} can be expressed as:

$$W_{iab} = \sum_{i=1}^{N} r_{ia} \cdot F_{ib} \tag{12}$$

where r_i is the position of ith atom and F_i is the total force acting on the ith atom due to interactions with other atoms. The virial stress of the

atom i has six components and can be written as:

$$\sigma_{iab} = \frac{S_{iab}}{V_i} \tag{13}$$

where the atomic volume V_i was determined by using Voronoi tessellation to partition the simulation box volume into each atom inside. The resulting atomic virial stress is then mapped to the appropriate bin on a grid. The representative stress value at each grid point was determined by averaging the stresses of all particles within the bin. It is important to note that only the normal stress components have been included in the calculation of atomic stress. Furthermore, the analysis has been restricted to atoms located within a 30 Å thickness regime around the dislocation slip plane.

Data availability
The data generated in this study are provided in the Supplementary Information and Source Data file. Source data are provided with this paper.

References

1. Taub, A. I. & Fleischer, R. L. Intermetallic compounds for high-temperature structural use. *Science* **243**, 616–621 (1989).
2. Senkov, O. N., Gorsse, S. & Miracle, D. B. High temperature strength of refractory complex concentrated alloys. *Acta Mater* **175**, 394–405 (2019).
3. Russell, A. M. Ductility in intermetallic compounds. *Adv. Eng. Mater.* **5**, 629–639 (2003).
4. Baker, I. A review of the mechanical properties of B2 compounds. *Mater. Sci. Eng. A* **192–193**, 1–13 (1995).
5. Koch, C. C. Intermetallic matrix composites prepared by mechanical alloying—a review. *Mater. Sci. Eng. A* **244**, 39–48 (1998).
6. Liu, C. T., George, E. P., Maziasz, P. J. & Schneibel, J. H. Recent advances in B2 iron aluminide alloys: deformation, fracture and alloy design. *Mater. Sci. Eng. A* **258**, 84–98 (1998).
7. Yeh, J. -W. et al. Nanostructured high-entropy alloys with multiple principal elements: novel alloy design concepts and outcomes. *Adv. Eng. Mater.* **6**, 299–303 (2004).
8. Cantor, B., Chang, I. T. H., Knight, P. & Vincent, A. J. B. Microstructural development in equiatomic multicomponent alloys. *Mater. Sci. Eng. A* **375–377**, 213–218 (2004).
9. George, E. P., Raabe, D. & Ritchie, R. O. High-entropy alloys. *Nat. Rev. Mater.* **4**, 515–534 (2019).
10. Miracle, D. B. & Senkov, O. N. A critical review of high entropy alloys and related concepts. *Acta Mater* **122**, 448–511 (2017).
11. Wang, H. et al. Multifunctional high entropy alloys enabled by severe lattice distortion. *Adv. Mater.* **36**, 2305453 (2024).
12. Yeh, J. W. Recent progress in high-entropy alloys. *Ann. Chim. Sci. Mater.* **31**, 633–648 (2006).
13. He, Q. F. et al. A highly distorted ultraelastic chemically complex Elinvar alloy. *Nature* **602**, 251–257 (2022).
14. Li, J. et al. Heterogeneous lattice strain strengthening in severely distorted crystalline solids. *Proc. Natl. Acad. Sci. USA* **119**, e2200607119 (2022).
15. Ye, Y. F. et al. Atomic-scale distorted lattice in chemically disordered equimolar complex alloys. *Acta Mater* **150**, 182–194 (2018).
16. Lu, W., Li, C., Yi, J. & Li, K. Stability and elastic properties of B2 CoX (X = Ti, Zr and Hf) intermetallic compounds as a function of pressure. *Philos. Mag.* **98**, 203–218 (2018).
17. Huang, X., Ackland, G. J. & Rabe, K. M. Crystal structures and shape-memory behaviour of NiTi. *Nat. Mater.* **2**, 307–311 (2003).
18. Du, J., Wen, B., Melnik, R. & Kawazoe, Y. First-principles studies on structural, mechanical, thermodynamic and electronic properties of Ni–Zr intermetallic compounds. *Intermetallics* **54**, 110–119 (2014).
19. Sheng, L. et al. Effect of Au addition on the microstructure and mechanical properties of NiAl intermetallic compound. *Intermetallics* **18**, 740–744 (2010).
20. Takasugi, T. & Izumi, O. Deformation of CoTi polycrystals. *J. Mater. Sci.* **23**, 1265–1273 (1988).
21. Lewandowski, J. J. & Greer, A. L. Temperature rise at shear bands in metallic glasses. *Nat. Mater.* **5**, 15–18 (2006).
22. Schuh, C. A., Hufnagel, T. C. & Ramamurty, U. Mechanical behavior of amorphous alloys. *Acta Mater* **55**, 4067–4109 (2007).
23. Wright, W. J., Schwarz, R. B. & Nix, W. D. Localized heating during serrated plastic flow in bulk metallic glasses. *Mater. Sci. Eng. A* **319–321**, 229–232 (2001).
24. Yang, Y., Ye, J. C., Lu, J., Liu, F. X. & Liaw, P. K. Effects of specimen geometry and base material on the mechanical behavior of focused-ion-beam-fabricated metallic-glass micropillars. *Acta Mater* **57**, 1613–1623 (2009).
25. Greer, J. R. & De Hosson, J. T. M. Plasticity in small-sized metallic systems: Intrinsic versus extrinsic size effect. *Prog. Mater. Sci.* **56**, 654–724 (2011).
26. Rizzardi, Q. et al. Mild-to-wild plastic transition is governed by athermal screw dislocation slip in bcc Nb. *Nat. Commun.* **13**, 1–9 (2022).
27. Bellón, B., Haouala, S. & LLorca, J. An analysis of the influence of the precipitate type on the mechanical behavior of Al - Cu alloys by means of micropillar compression tests. *Acta Mater* **194**, 207–223 (2020).
28. Zhang, Y. et al. Serration and noise behaviors in materials. *Prog. Mater. Sci.* **90**, 358–460 (2017).
29. Darolia, R. et al. Overview of NiAl alloys for high temperature structural applications. In *Ordered Intermetallics—Physical Metallurgy and Mechanical Behaviour* (eds Liu, C.T., Cahn, R.W. & Sauthoff, G.) 679–698 (Springer Netherlands, 1992).
30. Tong, Y. et al. Severe local lattice distortion in Zr- and/or Hf-containing refractory multi-principal element alloys. *Acta Mater* **183**, 172–181 (2020).
31. Lu, Y., Zhang, Y. H., Ma, E. & Han, W. Z. Relative mobility of screw versus edge dislocations controls the ductile-to-brittle transition in metals. *Proc. Natl. Acad. Sci. USA* **118**, 1–6 (2021).
32. Rao, S. I. et al. Atomistic simulations of dislocations in a model BCC multicomponent concentrated solid solution alloy. *Acta Mater* **125**, 311–320 (2017).
33. Lee, C. et al. Strength can be controlled by edge dislocations in refractory high-entropy alloys. *Nat. Commun.* **12**, 6–13 (2021).
34. Maresca, F. & Curtin, W. A. Mechanistic origin of high strength in refractory BCC high entropy alloys up to 1900K. *Acta Mater* **182**, 235–249 (2020).
35. Wang, F. et al. Multiplicity of dislocation pathways in a refractory multiprincipal element alloy. *Science* **370**, 95–101 (2020).
36. Lin, Y. S., Cak, M., Paidar, V. & Vitek, V. Why is the slip direction different in different B2 alloys? *Acta Mater* **60**, 881–888 (2012).
37. Chang, Z., Hu, J., Hu, G., Tao, R. & Wang, Y. Controlling elastic waves with isotropic materials. *Appl. Phys. Lett.* **98**, 121904 (2011).
38. Yamaguchi, M., Inui, H. & Ito, K. High-temperature structural intermetallics. *Acta Mater* **48**, 307–322 (2000).
39. Stoloff, N. S., Liu, C. T. & Deevi, S. C. Emerging applications of intermetallics. *Intermetallics* **8**, 1313–1320 (2000).
40. Nishibata, T. & Kojima, N. Effect of quenching rate on hardness and microstructure of hot-stamped steel. *J. Alloys Compd.* **577**, S549–S554 (2013).
41. Williams, D. B. & Carter, C. B. Spatial resolution and minimum detection. In *Transmission Electron Microscopy: A Textbook for Materials Science* 663–677 (Springer US, 2009).
42. Hÿtch, M. J., Snoeck, E. & Kilaas, R. Quantitative measurement of displacement and strain fields from HREM micrographs. *Ultramicroscopy* **74**, 131–146 (1998).

43. Han, Z., Wu, W. F., Li, Y., Wei, Y. J. & Gao, H. J. An instability index of shear band for plasticity in metallic glasses. *Acta Mater* **57**, 1367–1372 (2009).

44. Brüning, R. & Samwer, K. Glass transition on long time scales. *Phys. Rev. B* **46**, 11318 (1992).

45. Thompson, A. P., Swiler, L. P., Trott, C. R., Foiles, S. M. & Tucker, G. J. Spectral neighbor analysis method for automated generation of quantum-accurate interatomic potentials. *J. Comput. Phys.* **285**, 316–330 (2015).

46. Nogueira, F. Bayesian optimization: open source constrained global optimization tool for Python. https://github.com/fmfn/BayesianOptimization (2014).

47. Kresse, G. & Furthmüller, J. Efficient iterative schemes for ab initio total-energy calculations using a plane-wave basis set. *Phys. Rev. B* **54**, 11169 (1996).

48. Kresse, G. & Furthmüller, J. Efficiency of ab-initio total energy calculations for metals and semiconductors using a plane-wave basis set. *Comput. Mater. Sci.* **6**, 15–50 (1996).

49. Blöchl, P. E. Projector augmented-wave method. *Phys. Rev. B* **50**, 17953 (1994).

50. Monkhorst, H. J. & Pack, J. D. Special points for Brillouin-zone integrations. *Phys. Rev. B* **13**, 5188 (1976).

51. Meyers, M. A. & Chawla, K. K. Elastic properties of materials. In *Mechanical Behavior of Materials* 110–120 (Cambridge University Press, 2008).

52. Thompson, A. P. et al. LAMMPS—a flexible simulation tool for particle-based materials modeling at the atomic, meso, and continuum scales. *Comput. Phys. Commun.* **271**, 108171 (2022).

53. Hirel, P. Atomsk: A tool for manipulating and converting atomic data files. *Comput. Phys. Commun.* **197**, 212–219 (2015).

54. Mosleh, A. et al. Automated identification and indexing of dislocations in crystal interfaces. *Model. Simul. Mater. Sci. Eng.* **20**, 085007 (2012).

55. Larsen, P. M., Schmidt, S. ø & SchiØtz, J. Robust structural identification via polyhedral template matching. *Model. Simul. Mater. Sci. Eng.* **24**, 055007 (2016).

56. Stukowski, A. Visualization and analysis of atomistic simulation data with OVITO–the open visualization tool. *Model. Simul. Mater. Sci. Eng.* **18**, 015012 (2009).

57. Choi, W. M., Jo, Y. H., Sohn, S. S., Lee, S. & Lee, B. J. Understanding the physical metallurgy of the CoCrFeMnNi high-entropy alloy: an atomistic simulation study. *NPJ Comput. Mater.* **4**, 1–9 (2018).

58. Rycroft, C. H. VORO++: a three-dimensional Voronoi cell library in C++. *Chaos* **19**, 041111 (2009).

59. Yin, S. et al. Atomistic simulations of dislocation mobility in refractory high-entropy alloys and the effect of chemical short-range order. *Nat. Commun.* **12**, 1–14 (2021).

Acknowledgements

Author contributions

Conceptualization: Y.Y. and C.W.P. Methodology: Q.F.H., H.W., P.Y.Y., C.W.P., and Y.Y. Investigation: H.W., P.Y.Y., W.J.Z., S.H.M., J.H.H., Q.F.H., Q.W., Q.C., B.S.G., J.C.Q., C.L.W., H.A.C., and C.T.L. Visualization: H.W., W.J.Z., P.Y.Y., and S.H.M. Funding acquisition: Y.Y., C.W.P., B.S.G., J.C.Q., W.J.L., and Q.F.H. Supervision: Y.Y. Writing—original draft: H.W., P.Y.Y., and S.H.M. Writing— review and editing: Y.Y., C.W.P., Y.L., W.J.L., S.J.Z., and X.D.X.

Competing interests

The authors declare no competing interests.

Additional information

Supplementary information The online version contains supplementary material available at https://doi.org/10.1038/s41467-024-51204-0.

Correspondence and requests for materials should be addressed to Y. Liu, C. W. Pao or Y. Yang.

Peer review information *Nature Communications* thanks Peyman Asghari-Rad, Marek Mihalkovic, Ravit Silverstein and the other, anonymous, reviewer(s) for their contribution to the peer review of this work. A peer review file is available.

Reprints and permissions information is available at http://www.nature.com/reprints

Publisher's note Springer Nature remains neutral with regard to jurisdictional claims in published maps and institutional affiliations.